

Solitary wave effects north of Strait of Messina

A. Warn-Varnas^{a,*}, J. Hawkins^b, P.K. Smolarkiewicz^c,
S.A. Chin-Bing^a, D. King^a, Z. Hallock^a

^a *Naval Research Laboratory, Stennis Space Center, MS 39529, USA*

^b *Planning Systems Inc., Slidell, LA 70458, USA*

^c *National Center for Atmospheric Research, Boulder, CO 80307, USA*

Received 11 January 2007; received in revised form 8 March 2007; accepted 9 March 2007

Available online 6 April 2007

Abstract

We present new results from a joint ocean-acoustic modeling study of solitary wave generation in the Strait of Messina, their propagation in the Tyrrhenian Sea and subsequent shoaling in the Gulf of Gioia. The nonhydrostatic 3D EULAG model is used for the oceanographic predictions. The simulations are initialized with measured temperature and salinity profiles from an October 1995 survey of the Messina region, and forced with semidiurnal tidal magnitudes predicted by a barotropic tidal model. Parameter sensitivity studies are performed. The predicted solitary wave trains are compared with CTD chain measurements. The model results and data are examined through a wavelet analysis. The wavelengths are tracked by the spines (maximum intensity for each wavelength) at various times. From the slope of the variations, phase speeds are derived as a function of wavelength. For the parameters extracted from CTD measurements and existing tidal conditions, phase speed distribution for wavelengths ranging from about 0.6 m to 1.6 km are obtained. The model predicted phase speed magnitudes range from 0.85 m s^{-1} to 0.93 m s^{-1} . The phase speeds derived from data range from 0.77 m s^{-1} to 0.88 m s^{-1} . The model predicted phase speed versus wavelength distribution has similar trends to the phase speed versus wavelength distribution derived from data. The shoaling of the solitary waves in the Gulf of Gioia is studied. Calculations of the acoustical field are conducted, along the solitary wave propagation path, with the parabolic (PE) acoustical model.

Published by Elsevier Ltd.

Keywords: Ocean models; Solitary waves; Barotropic tide; Messina sill; Wavelet analysis; CTD chain data

1. Introduction

The Strait of Messina connects the Tyrrhenian Sea, on the north side, and the Ionian Sea, on the south side. Fig. 1 shows the area of interest, with bathymetric contours in meters. The strait contains a sill that raises to

* Corresponding author.

E-mail address: varnas@nrlssc.navy.mil (A. Warn-Varnas).

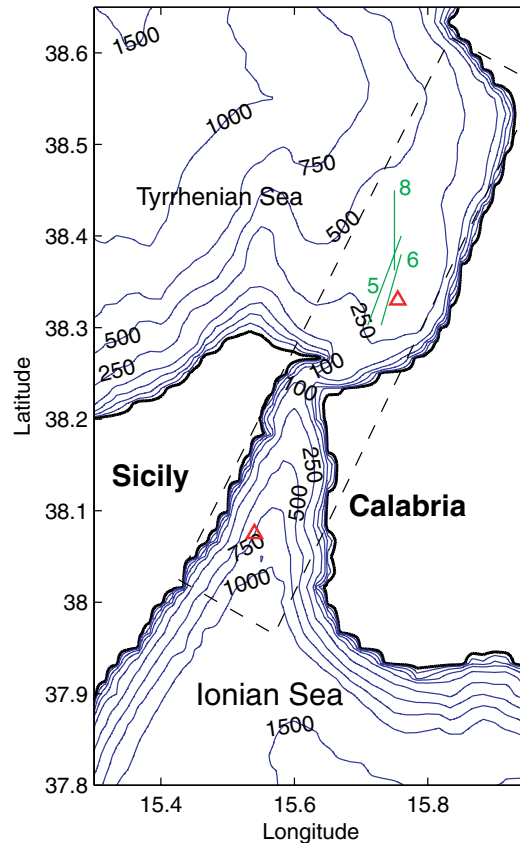


Fig. 1. Strait of Messina and Gulf of Gioia region. Triangles are CTD stations. CTD chain tracks 5, 6, and 8 are indicated (green curve). The dashed box shows the horizontal model domain.

within 80 m of the surface at the shallowest point. The water masses of the Ionian and Tyrrhenian Seas mix in the strait. On the north side of the strait (towards the Gulf of Gioia), the depth increases, reaches a maximum and then decreases.

One of the first attempts to explain the tidal dynamics of the Straits of Messina was by [Sterneck \(1915\)](#). He proposed a pattern of tidal oscillations, in the Strait of Messina, generated by the M2 semi-diurnal tide and obtained numerical solutions of the linear tidal equations. [Vercelli \(1925\)](#) conducted a survey of the Strait of Messina and concluded that the current distribution is largely due to tidal action. He showed that there is a large gradient of tidal amplitude between the tides north and south of the sill because the tides are out of phase by about 180°. Because of the phase opposition and the topographic constrains the tidal currents can reach magnitudes of around 3 m s^{-1} . The magnitudes of these currents were known in ancient times, dating back to Homer's *Odyssey* ([Alpers and Salusti, 1983](#)). The advent of the SEASAT satellite has brought forth new information on the oceanography of the strait. Analysis of the SEASAT SAR data showed the presence of internal waves that were linked to tidal currents moving over the Messina sill ([Alpers and Salusti, 1983](#)).

The generation and subsequent propagation of solitary waves over topographic changes – e.g., at shelf-breaks or sills – has been modeled with nonhydrostatic hydrodynamic models. The hydrodynamic modeling of tidal flow over steep topography shows that the tidal flow depresses the pycnocline and generates an internal bore ([Lamb, 1994](#); [Brand et al., 1997](#); [Warn-Varnas et al., 2003](#)). The internal bore propagates and its leading edge steepens through nonlinear effects. Then frequency and amplitude dispersion sets in, and the leading edge disintegrates into propagating solitary waves ([Lamb, 1994](#); [Brand et al., 1997](#); [Warn-Varnas et al., 2003](#)). In particular, the interaction of the Strait of Messina sill with the semidiurnal tidal motion results in the formation of internal bores. As the semidiurnal tidal motion reverses itself, the internal bores undergo a

hydraulic jump over the sill. Internal bore depressions are most pronounced in the thermocline and halocline regions. During the jump of an internal bore over the sill, temperature and salinity fronts are formed. These fronts separate the water masses in the lower and upper parts. The interface between the two water masses has been investigated in Hopkins et al. (1984) and Del Ricco (1981).

The propagating solitary wave trains are seen as evidence of an isopycnal depression (Osborne and Burch, 1980). The depressions associated surface convergence and divergence patterns have been observed in SAR imagery (Alpers and Salusti, 1983). The isotherm displacements can be measured with a towed CTD thermistor chain (Sellschopp, 1997). The propagating solitary wave trains undergo dispersion in amplitude, wavelength, and phase speed (Brand et al., 1997; Warn-Varnas et al., 2003). On the north side of the sill the internal solitary waves propagate towards the Gulf of Gioia. In the Gulf of Gioia the solitary waves shoal as the topography raises toward the surface. The JANE 1984 (Guardiani et al., 1988; JANE, 1985) cruise measurements indicated a patch of mixed water between 40 m and 100 m that could be caused by mixing due to the shoaling of internal solitary waves.

In this study, we model numerically the three-dimensional oceanographic structure from the Messina Strait sill to the Gulf of Gioia. This encompasses the channel for the Messina sill into the Ionian Sea and the Tyrrhenian Sea into the Gulf of Gioia. Our objectives are to study the characteristics and effects of solitary waves embedded in a three-dimensional structure during generation, propagation, and shoaling. The numerical model is initialized from a survey of the region, conducted in October 1995, and the characteristics of the predicted solitary trains are compared against CTD chain measurements. Effects of oceanographic parameter variations on solitary wave characteristics are studied. The variations of oceanographic parameters are related to the characteristics of solitary wave trains measured with the CTD chain. The shoaling of the solitary waves in the Gulf of Gioia is studied.

The temporal and spatial scales of tidally induced internal bores and solitary waves are such that they can have a significant effect on the acoustic field through the sound speed structure. At certain frequencies the interaction of the acoustic field with the solitary waves can be quite significant. Many interactions of the acoustical field with the solitary wave train can occur between the source and the receiver (Warn-Varnas et al., 2003).

The paper is organized as follows. The following section briefly characterizes the data that drive the numerical model summarized in Section 3 and Appendix. Section 4 discusses ocean dynamics simulated by the model; whereas the validation of the model results, using comparisons with measurements and parameter-sensitivity study, is presented in Section 5. Section 6 discusses acoustical effects, and the summary of our conclusions is presented in Section 7.

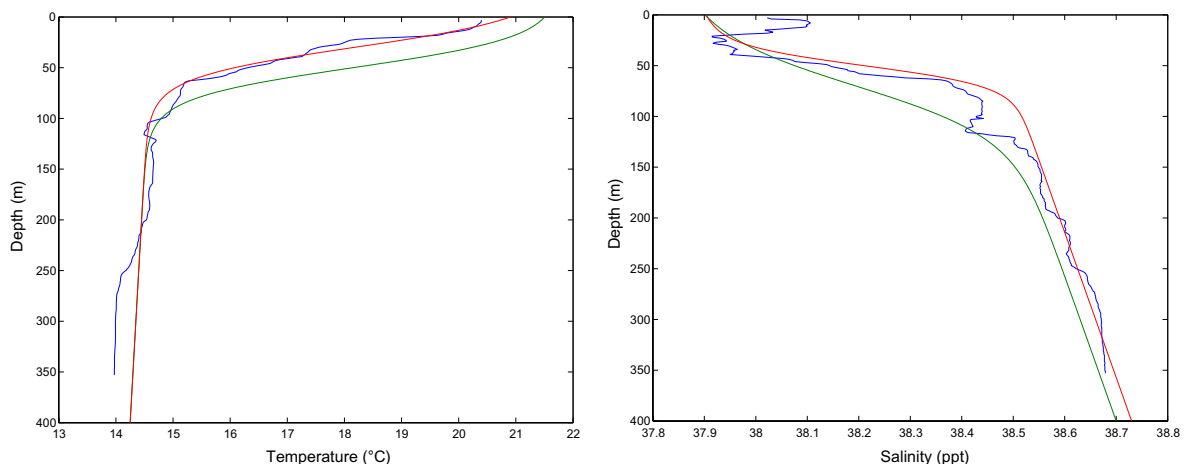


Fig. 2. Measured (blue) and fitted (red and green; case 1 and 3 in Table 1 of Section 4.1, respectively) ambient profiles of temperature (left plate) and salinity (right plate).

2. Data

In October of 1995 a survey of the Atlantic Ionian Stream was conducted in the Strait of Sicily. At the end of this sea trial, on October 24 and 25, solitary wave trains were tracked in the Strait of Messina with a towed conductivity–temperature–depth (CTD) chain (Sellschopp, 1997). The chain had 83 sensors attached on a 270 m cable. The accuracies of the sensors were 0.01 K for temperature and 0.02 ppt for salinity. The resultant horizontal and vertical resolution was 5 m and 2.5 m at a ship speed of 2.5 m s^{-1} (Sellschopp, 1997).

On the Tyrrhenian Sea side, tows 5, 6, and 8 (shown as green lines in Fig. 1) passed through the same packet. The CTD chain measurements were corrected for ship motion. From the measured temperature and salinity values, Fig. 2, the densities and sound speeds were calculated.

3. Model

3.1. Overview

The numerical predictions were conducted with the nonoscillatory forward-in-time (NFT)¹ model, termed EULAG for its capability to solve the fluid equations in either an Eulerian (flux-form) or a Lagrangian (advective form) mode (see Smolarkiewicz and Prusa, 2002, for a succinct review). The default analytic formulation of EULAG assumes the nonhydrostatic anelastic equations of motion, with options available for compressible/incompressible Boussinesq, and incompressible Euler/Navier–Stokes equations (Smolarkiewicz et al., 2001). The ocean derivative of EULAG developed for the purpose of this study builds on the classical incompressible Boussinesq approximation that enables efficient semi-implicit integrations of stiff governing equations supporting gravity waves on a broad range of scales. The resulting NFT ocean model retains all multiscale benefits of the EULAG’s mathematical/numerical design, widely documented in the literature. Among others, these include: (i) formulation and solution of governing PDEs in generalized time-dependent curvilinear coordinates, admitting grid adaptivity to flow features and/or irregular boundaries (Prusa and Smolarkiewicz, 2003; Wedi and Smolarkiewicz, 2004; Smolarkiewicz and Prusa, 2005; Prusa and Gutowski, 2006); and (ii) the direct numerical simulation (DNS), large-eddy simulation (LES), and implicit large-eddy simulation (ILES) turbulence modeling capabilities, facilitating applications at broad range of Reynolds numbers (Smolarkiewicz and Prusa, 2002; Smolarkiewicz and Margolin, 2007).

For clarity, we present only the adiabatic meso-scale model equations, and dismiss the physical forcing other than buoyancy, pressure, and Coriolis. The following discussion thus conveys only a small portion of the EULAG’s capabilities, but the summarized methodology is representative of the entire model. Further, given the physical scope of this paper we use a concise symbolic operator-form description of the governing equations; for the complete tensorial expositions refer to Smolarkiewicz and Prusa (2005) and references therein.

3.2. Analytic formulation

To address a broad class of flows in a variety of domains – with, optionally, Dirichlet, Neumann, or periodic boundaries in each direction – we formulate (and solve) the governing equations in a *transformed* domain with time-dependent curvilinear coordinates

$$(\bar{t}, \bar{\mathbf{x}}) \equiv (t, \mathcal{F}(t, \mathbf{x})). \quad (1)$$

The key assumptions are that the coordinates (t, \mathbf{x}) of the *physical* domain are orthogonal and stationary – in particular, Cartesian in this paper – and that the transformed horizontal coordinates (\bar{x}, \bar{y}) are independent of the vertical coordinate z . Given the transformation in (1), the adiabtic incompressible Boussinesq equations for a salty water can be compactly written as follows:

¹ The acronym NFT labels a class of second-order-accurate two-time-level algorithms built on nonlinear advection techniques that suppress/reduce/control numerical oscillations characteristic of higher-order linear schemes; it is meant to distinguish these algorithms from classical centered-in-time-and-space linear methods.

$$\bar{\nabla} \cdot (\rho^* \bar{\mathbf{v}}^s) = 0, \quad (2)$$

$$\frac{d\mathbf{v}}{d\bar{t}} = -\tilde{\mathbf{G}}(\bar{\nabla}\pi') + \mathbf{g} \frac{\rho'}{\rho_0} - \mathbf{f} \times \mathbf{v}', \quad (3)$$

$$\frac{d\rho'}{d\bar{t}} = -\bar{\mathbf{v}}^s \cdot \bar{\nabla}\rho_e, \quad (4)$$

$$\frac{ds}{d\bar{t}} = 0, \quad (5)$$

where, because of the coordinate transformation, the physical and geometrical aspects intertwine each other. Insofar as the physics is concerned: $\mathbf{v} \equiv [u, v, w]$ denotes the *physical velocity* vector; ρ , s and π denote density, specific salinity, and a density-normalized pressure; \mathbf{g} is the acceleration of gravity (vector), and \mathbf{f} the vector of Coriolis parameter. Primes denote deviations from the geostrophically-balanced ambient (alias, environmental) state \mathbf{v}_e , ρ_e ; and ρ_0 is the Boussinesq reference density.

The geometry of the coordinates in (1) enters the governing equations as follows: in the mass continuity Eq. (2), $\rho^* \equiv \rho_0 \bar{G}$ with \bar{G} denoting the Jacobian of the transformation; whereas in the momentum Eq. (3), $\tilde{\mathbf{G}}$ symbolizes the renormalized Jacobi matrix of the transformation coefficients $\sim (\partial \bar{\mathbf{x}} / \partial \mathbf{x})$; $\bar{\nabla} \cdot \equiv \partial / \partial \bar{\mathbf{x}}$, and the total derivative is given by $d/d\bar{t} = \partial / \partial \bar{t} + \bar{\mathbf{v}}^* \cdot \bar{\nabla}$, where $\bar{\mathbf{v}}^* \equiv d\bar{\mathbf{x}}/d\bar{t} \equiv \dot{\bar{\mathbf{x}}}$ is the *contravariant velocity*. Appearing in the continuity (2) and density (4) equations is a weighted *solenoidal velocity*

$$\bar{\mathbf{v}}^s \equiv \bar{\mathbf{v}}^* - \frac{\partial \bar{\mathbf{x}}}{\partial \bar{t}}, \quad (6)$$

which readily follows (Prusa et al., 2001) from the generic (tensor invariant) form of the mass continuity equation

$$\bar{G}^{-1} \left(\frac{\partial \rho^*}{\partial \bar{t}} + \bar{\nabla} \cdot (\rho^* \bar{\mathbf{v}}^*) \right) \equiv 0. \quad (7)$$

Use of the solenoidal velocity facilitates the solution procedures because it preserves the incompressible character of numerical equations, regardless of the time-dependency of the transformed coordinates. While numerous relationships can be derived that express any velocity (solenoidal, contravariant, covariant, or physical) in terms of the other, in either transformed or physical coordinate system, a particularly useful transformation

$$\bar{\mathbf{v}}^s = \tilde{\mathbf{G}}^T \mathbf{v}. \quad (8)$$

relates the solenoidal and physical velocities directly. For further details of the metric and transformation tensors as well as formulating viscous and dissipative terms in the governing equations, the interested reader is referred to Smolarkiewicz and Prusa (2005) and the references therein.

The equations of motion (2)–(5) are supplemented with a linearized constitutive law for sea water

$$\rho' = \alpha T' + \beta s' \quad (9)$$

with constants $\alpha = -2.5 \times 10^{-4}$ and $\beta = 7.6 \times 10^{-4}$, representative of conditions in the Mediterranean region (Benoit, 1994; Marshall et al., 1997). The linear relation (9) is used to diagnose temperature/potential-temperature perturbations and to construct the ambient density profile ρ_e from the potential temperature and salinity profiles θ_e and s_e .

The numerical apparatus employed to solve the posed equations is summarized in Appendix. Here we note that there are four important benefits of formulating governing PDEs as described: (i) the relative simplicity of designing a flow solver fully implicit with respect to gravity waves (Appendix); (ii) conservation of density perturbations with accuracy to round-off error – cf. Section 3a in Smolarkiewicz et al. (2001), for a discussion – tantamount to preventing dilution of the ambient stratification due to implicit viscosity of nonoscillatory advection; (iii) improved accuracy of impermeability conditions imposed along irregular boundaries (Smolarkiewicz et al., 2001); and (iv) improved energetics of the model (Wedi, 2006). For a validation against an akin laboratory experiment with density stratification and transient nonlinear gravity-wave dynamics see Wedi and Smolarkiewicz (2006).

3.3. The model setup: details of transformation

Following Wedi and Smolarkiewicz (2004), the general dependence of \bar{z} on (x, y, z, t) in (1) collapses into a similarity transformation

$$\begin{aligned}\bar{z} &= \mathcal{C}(\xi) \\ \xi &= \xi(x, y, z, t) := H_0 \frac{z - z_s(x, y, t)}{H(x, y, t) - z_s(x, y, t)},\end{aligned}\tag{10}$$

where H and z_s are the upper and lower surface elevations, respectively, H_0 denotes the vertical extent of the transformed model domain, and the function \mathcal{C} conveniently admits a class of vertically stretched coordinates. The transformation in (10) is a generalization of the classical terrain-following Gal-Chen and Somerville (1975) transformation. It has the computational advantage of separability into one- and two-dimensional fields. In particular, the Jacobian of the transformation is given as

$$\begin{aligned}\bar{G} &= \left(\frac{d\mathcal{C}}{d\xi} \frac{\partial \xi}{\partial z} \right)^{-1} \left(\frac{\partial \bar{x}}{\partial x} \frac{\partial \bar{y}}{\partial y} - \frac{\partial \bar{x}}{\partial y} \frac{\partial \bar{y}}{\partial x} \right)^{-1} \\ &\equiv \left(\frac{d\mathcal{C}}{d\xi} \right)^{-1} \bar{G}_0 \bar{G}_{xy},\end{aligned}\tag{11}$$

with

$$\bar{G}_0 \equiv \left(\frac{\partial \xi}{\partial z} \right)^{-1} = \frac{H(x, y, t) - z_s(x, y, t)}{H_0}.\tag{12}$$

The similarity transformation (10) is a convenient vehicle for bringing a varying ocean surface from other sources, either data or models. For illustration see Wedi and Smolarkiewicz (2004), where the authors simulated nonhydrostatic flow of a homogeneous shallow layer of water past a hill, with a variable upper boundary $H(x, y, t)$ in (10) predicted by integrating the shallow-water equations. Furthermore, the dependence of \bar{x} and \bar{y} on the horizontal coordinates of the physical space, admits studies of fluid flows in curved channels (Smolarkiewicz and Prusa, 2005). Notwithstanding the generality of (10), throughout this paper $\bar{x} = x$, $\bar{y} = y$ and $\xi = \bar{z}$; thereby employing the identity transformation in the horizontal (viz. $\bar{G}_{xy} \equiv 1$). Furthermore, the upper boundary is stationary and flat (viz. $H \equiv H_0$), and there is no vertical stretching of the lower-boundary-fitted coordinate \bar{z} (viz. $d\mathcal{C}/d\xi \equiv 1$). The lower boundary is also stationary but inhomogeneous, $z_s = z_s(x, y)$, thereby reducing (10) to the classical case, standard in many atmospheric/oceanic models. In spite of the resulting mathematical simplifications, the actual EULAG program accommodates (1) and (10) in their full generality. Consequently, we retain the consistent notation for future reference and ease of connection to earlier works.

3.4. The model setup: ambient, initial and boundary conditions

A specific perturbation form of PDEs solved in EULAG depends on the admitted class of ambient states. Consider for illustration that the governing system (2)–(5) derives from the generic Boussinesq form – in which the pressure and temperature perturbations in the momentum equation are taken with respect to the static vertical profiles of the Boussinesq expansion – simply by postulating there exists an *inertial* ambient state determined by the balance of pressure, buoyancy, and Coriolis forces

$$0 = -\tilde{\mathbf{G}}(\bar{\nabla}(\pi_c - \pi_0)) + \mathbf{g} \frac{\rho_c - \rho_0}{\rho_0} - \mathbf{f} \times \mathbf{v}_c,\tag{13}$$

together with implied compatibility conditions (e.g., for a sheared ambient flow, ρ_c must change accordingly in the horizontal; cf. Smolarkiewicz et al., 2001, for a discussion). Subtracting (13) from the generic form results in (3), while the perturbational formulation of the density Eq. (4) follows readily the generic form $d\rho/d\bar{t} = 0$, given $\rho_c = \rho_c(\mathbf{x})$.

This feature of the model is employed to incorporate the effects of tidal forcing. In particular, the ambient flow is assumed as $\mathbf{v}_e = [u_e(t), 0, 0]$, where

$$u_e = V_T \cos\left(\frac{2\pi}{T}t\right). \quad (14)$$

Here, constant V_T denotes the flow magnitude at the south boundary of the model located on the Ionian side of the Messina Strait, with numerical value (Table 1) determined after Martin (2000); whereas $T = 12.4$ h is the semidiurnal period of the tidal forcing. Because the ambient flow is allowed to vary in time, the governing momentum equations should include $\partial \mathbf{v}_e / \partial t$ on the rhs – in light of the preceding discussion. However, since the characteristic time-scale of solitary-wave evolution is much shorter than T , these terms are neglected in further discussion. The perturbation form of the governing equations is incapable per se of appreciating the tidal flow, as it is simply a result of subtracting a prescribed subset of solutions from both sides of the complete Boussinesq problem. The system is actually connected to tidal flow via inflow boundary conditions $\mathbf{v} \cdot \mathbf{n} = V_T$ imposed at the south inflow boundary, determining there the Neumann boundary condition for pressure in the elliptic boundary value problem (Appendix). In order to account for the sign-change of the tide after $T/2$, at the time of the model initialization the constant \widehat{V}_T is determined at the north lateral model boundary, such as to satisfy the integrability condition $\int_{\partial\Omega} \rho^* \widehat{\mathbf{v}}^s \cdot \mathbf{n} d\sigma = 0$ implied by (2). As the tide changes sign and the south and north boundaries become outflow and inflow, respectively, the solution accounts for the tide via $\mathbf{v} \cdot \mathbf{n} = \widehat{V}_T$ enforced at the north boundary. To minimize numerical-boundary artifacts, dissipative absorbing layers attenuate the solution gradually towards the ambient flow in the vicinity of the boundaries.

To ensure a well-posed initial condition (cf. Temam, 2006), $\mathbf{v}(t = 0)$ is assumed a superposition of the ambient flow and potential perturbation

$$\mathbf{v}(t = 0) = \mathbf{v}_e(t = 0) - \widetilde{\mathbf{G}}(\overline{\nabla}\phi), \quad (15)$$

and it is determined by solving (on the model grid) a discrete elliptic problem, for the potential ϕ , implied by the mass continuity equation (2) and the imposed boundary conditions. The initial fields of potential temperature and salinity are set to ambient values; whereupon, the initial density perturbation is set to zero. To construct the initial profiles, the ambient temperature and salinity fields were obtained from CTD stations shown in Fig. 1. For modeling convenience, analytic functions were fitted to the measurements, as shown Fig. 2.

The model domain of $L_x \times L_y \times H = 80 \times 10 \times 0.4$ km³ in x , y and z , respectively, is covered with $800 \times 100 \times 100$ grid points. The vertical extend is restricted to the top 400 m of the ocean. The x -direction is oriented from the Strait of Messina towards the Gulf of Gioia; consult Fig. 1 for the outline of the horizontal domain. Numerical simulations cover 2–5 semidiurnal tidal periods using time step δt of 1.5 s limited by the advective CFL condition. The $z = z_s$ and $z = H$ boundaries are impermeable. At $x = 0$ the lateral boundary is open, whereas at $x = L_x$ the bathymetry $z_s(x, y)$ continues into the coastline. To prevent a singularity in the transformation (10) where the bathymetry protrudes to the ocean surface $z = H$, the actual bathymetry is limited such that $z_s = \min(z_s, H - \Delta)$ with $\Delta = 20$ m; cf. Fig. 3. Concomitantly, in the sea region above the maximum bathymetry $z_{s\max} = H - \Delta$, flow is attenuated rapidly to stagnation using the Rayleigh friction (on the rhs of the momentum equation) – in the spirit of gravity-wave absorbers common in atmospheric models – with the e-folding time scale $\tau = 18$ s. At the $y = L_y$ model boundary, for all $x < 0.5L_x$ and $z > z_s$ the coastline is steep, thus justifying the approximation with impermeable vertical walls. At $y = L_y$ and $x \geq 0.5L_x$ the boundary is open for all $z > z_s$. The latter results in a complex shape of the opening towards Tyrrhenian Sea – an intersection of the (x, z) plane at $y = L_y$ with the bathymetry. This motivates the customized scheme

Table 1

Simulation parameters: the center of the thermocline depth P_T , the center of the halocline depth P_S , and the semidiurnal tidal magnitude

Case	P_T [m]	P_S [m]	V_T [m s ⁻¹]
1	40	50	0.5
2	40	50	0.25
3	60	70	0.5

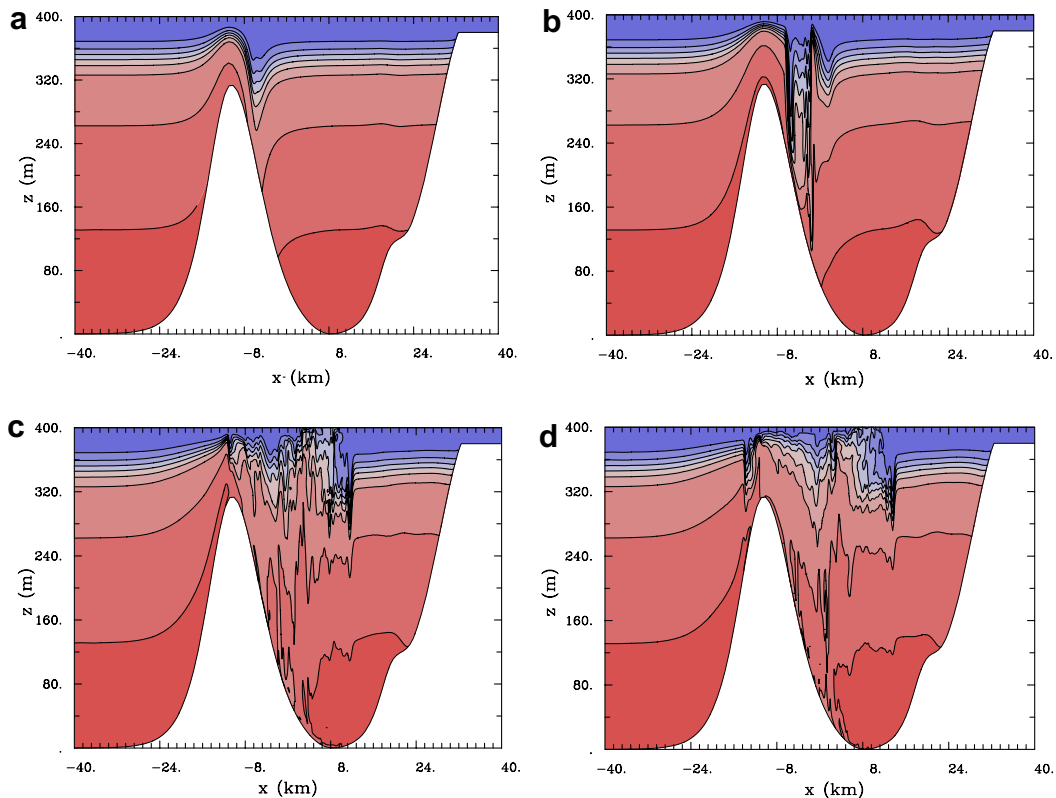


Fig. 3. Strait of Messina sill with Tyrrhenian Sea on the right and Ionian Sea on the left. Isohalines contours from 37.995 ppt to 38.638 ppt in intervals of 0.09 ppt in the $y = 5$ km xz plane at: (a) 0.52 h; (b) 1.55 h; (c) 3.62 h and (d) 4.13 h.

for handling the tide reversal, discussed earlier in this subsection. At $y = 0$ the boundary is impermeable for all $z > z_s$, and the narrowing of the channel at the sill is represented by the bathymetry, analogously to the $x = L_x$ boundary; cf. Fig. 7a.

All calculations reported in this paper are performed using the Eulerian flux-form option of EULAG, executed in the ILES mode, in which the truncation terms of nonoscillatory transport schemes play the sole role of the subgrid-scale turbulence models; see Smolarkiewicz and Margolin (2007) for a review.

4. Dynamics

4.1. Generation of internal bores, fronts and solitary waves

At the Strait of Messina sill region, the salty water originates from Levantine Intermediate Water (LIW). The surface water can consist of modified atlantic water (MAW) or Tyrrhenian Sea surface water (TSW). As the semidiurnal tide moves over the Strait of Messina sill from the Ionian to the Tyrrhenian Sea, the pycnocline and halocline region is moved upwards at the sill and depressed on the right side of the sill, Fig. 3a. The depression is an internal bore with salinity and temperature gradients along its boundaries. The first internal bore to be formed by the tidal flow to the right, generates a right and a left propagating internal wave. The salinity field for such an internal bore is shown in Fig. 3a at the simulation time $t = 0.52$ h along a vertical xz plane located at mid distance along the y coordinate, $y = 5$ km. The parameters of the simulation are listed as case 1 in Table 1, where P_T is the center of the thermocline depth, P_S is the center of the halocline depth, and V_T is the prescribed semidiurnal tidal magnitude (cf. Section 3.4 for discussion). At $t = 1.55$ h, Fig. 3b, the right propagating wave steepens on the leading edge through nonlinear effects. Then, later in time, frequency

and amplitude dispersion set in and it disintegrates into solitary waves, Figs. 3c and 3d. These are solitary waves of depressions that push the isohalines, isotherms and isopycnals down. When the semidiurnal tidal flow reverses the direction, from positive to negative along x , the left propagating internal bore of depression that was formed by the positive tidal flow, Fig. 3b, undergoes a hydraulic jump over the sill, Figs. 3c and 3d.

Inside the internal bore, Figs. 3c and 3d, there is a tendency for a more homogeneous temperature and salinity distribution. At the bottom, left and right sides of it there are large salinity and temperature gradients – the temperature field has a similar distribution to the salinity field. As the bore moves over the sill, the bottom part generates a front between the surface and the top of the sill. During the dynamics of the motion that takes place over the semidiurnal tidal cycle, a large salinity and temperature gradient can be located anywhere between the sill and the surface of the ocean. The water masses that exist in the lower and upper parts of the sill region, are separated by this frontal temperature and salinity gradient. At $t = 6.2$ h the salinity distributions has evolved to the configuration shown in Fig. 4a.

There is a salinity gradient or front located past the mid depth over the sill. The two water masses, upper and lower, are on each side of the front. The internal bore that jumped over the sill, Fig. 3d, has now moved close to the $x = -24$ km location and has become steep on the leading side through nonlinear effects. Proceeding to $t = 7.75$ h the flow over the sill is moving to the left, towards the Ionian Sea. As the tidal flow continues to the left, the salinity front moves further up on the sill towards the surface. The gradient, associated with the front, is now located near the surface, Fig. 4b. To the right of the sill, the solitary wave train that was previously near $x = 24$ km, Fig. 4a, is heading towards the Gulf of Gioia, Fig. 4b.

The location of the salinity front changes as one proceeds westward from the mid plane (at $y = 5$ km) towards increasing y values. In a vertical plane close to the Sicilian shore, $y = 8$ km, at the time of 7.75 h the front is anchored on the left side of the sill and extends to the surface with a upwards slope, Fig. 5a. When the tidal flow reverses to be along the positive x -direction, at $t = 11.37$ h, the front becomes anchored on the right side of the sill and extends to the surface by sloping upwards to the left, Fig. 5b. The low salinity water tends to be on the right side of the front and the high salinity water on the left. In the previous case, Fig. 5a, the reverse situation existed. The solitary wave train that was located at $x = 24$ km in Fig. 5a at $t = 7.75$ h, has reached the Gulf of Gioia shore at $t = 11.37$ h, shoaled, and resulted in a depression along the shelfbreak, Fig. 5b.

Hopkins et al. (1984) and Del Ricco (1981) have investigated the time evolution of the interface between the two water masses over the Messina sill with two-layer models. The interface of the two-layer models was found to exhibit large vertical oscillations between the surface and bottom of the sill region. The interface can be at the surface, bottom or anywhere in-between. Our simulation with the nonhydrostatic model exhibit a similar phenomena of water mass separation by a frontal gradient of temperature and salinity caused by the semidiurnal tidal motion over the sill.

The solitary waves trains propagate away from the sill. The structure of the solitary waves changes along and across the direction of propagation. Consider a vertical section located towards the outer boundary in the

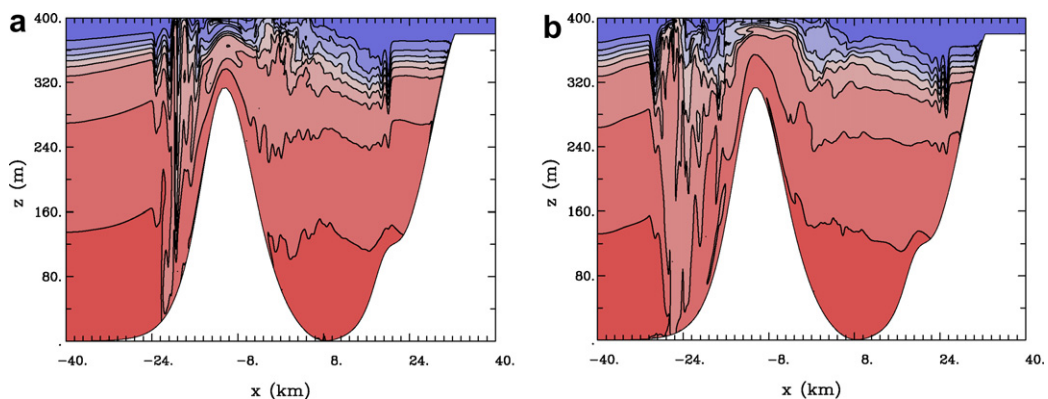


Fig. 4. Isohalines contours from 37.975 ppt to 38.636 ppt in intervals of 0.094 ppt in the $y = 5$ km xz plane at: (a) 6.2 h and (b) 7.75 h.

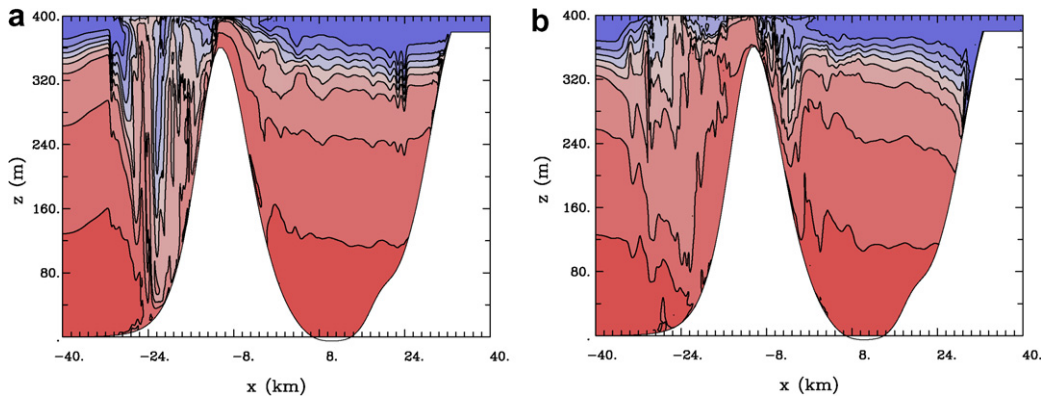


Fig. 5. Isohalines contours from 37.993 ppt to 38.642 ppt in intervals of 0.092 ppt in a xz plane at $y = 8$ km at: (a) $t = 7.75$ h and (b) $t = 11.37$ h.

y -direction, Fig. 5a. The beginning of the solitary wave train at $t = 7.75$ h is near $x = 24$ km. Along the mid section of the y -direction, Fig. 4b, the solitary wave train is located past $x = 24.0$ km, which is further ahead in the x -direction. As one moves across the direction of propagation in the y -direction, there is a curvature effect in the location of the solitary wave trains. The curvature of the solitary wave train can be seen in a horizontal plane located 100 m below the surface, Fig. 6. At around 65 km down range there is a warmer temperature distribution generated by the depressions associated with the solitary waves. These depressions bring the warmer surface temperature down. Note the curvature of the warmer temperature arcs. The arcs curve backwards, as one proceeds from land (bottom) towards the open sea (top).

4.2. Flow structure

At $t = 7.75$ h consider the semidiurnal tidal circulation that exists in the numerical domain. The forcing of the semidiurnal barotropic flow, Eq. (14) in Section 3.4, is in the reverse direction at this time. In the sill region

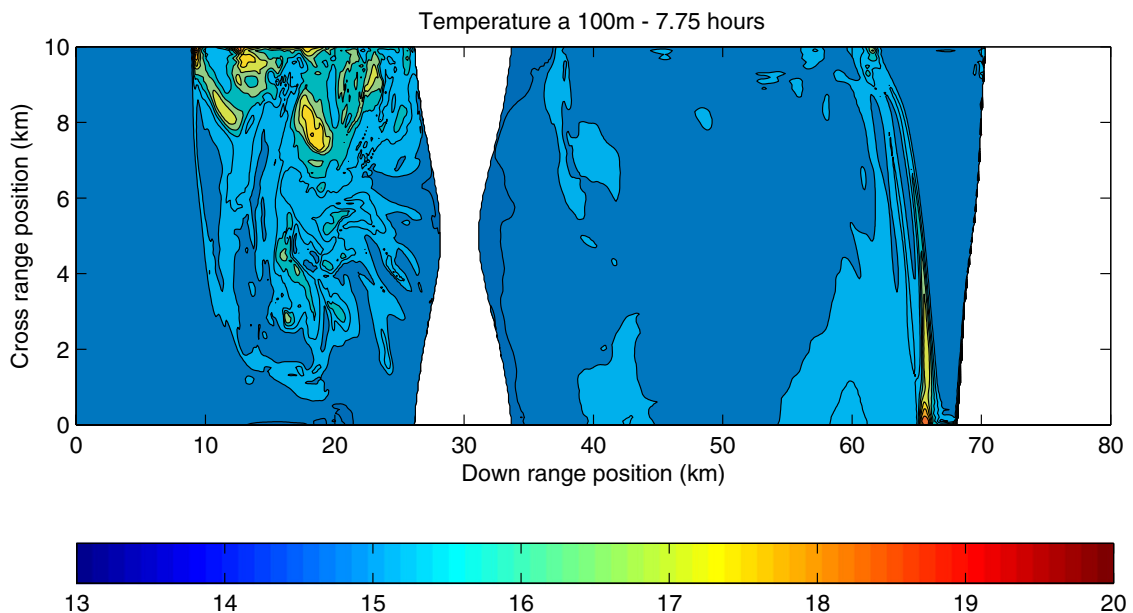


Fig. 6. Horizontal temperature distribution at 7.75 h in a plane located 100 m below the surface. Down range corresponds to the x -direction and cross-range to the y -direction.

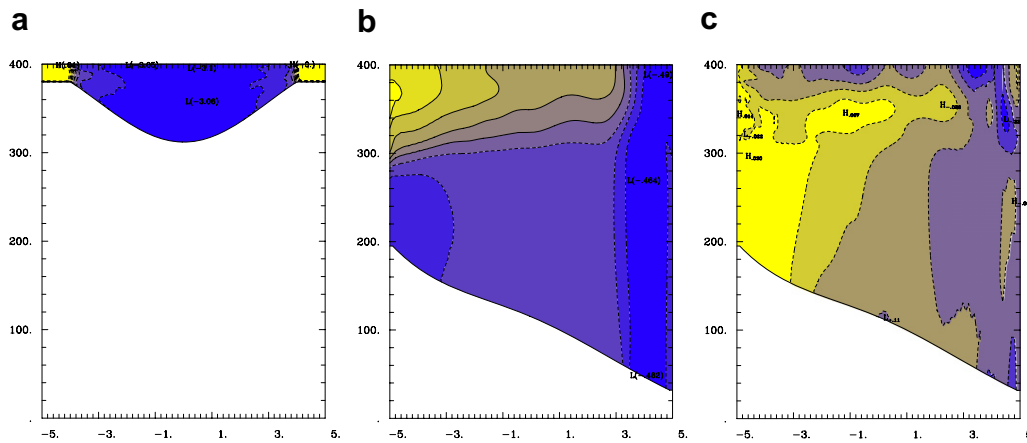


Fig. 7. Horizontal components of velocity at $t = 7.75$ h: (a) u component in the yz plane at 30 km down range of Fig. 6 with contours from -2.75 to -0.33 m s^{-1} in intervals of 0.04 m s^{-1} ; (b) u component at the 60 km down range with contours from -0.363 to $+0.53$ m s^{-1} in intervals of 0.128 m s^{-1} and (c) v component in the same plane as (b) with contours from -0.203 to -0.013 m s^{-1} in intervals of 0.047 m s^{-1} . Vertical and horizontal axes are marked in m and km, respectively.

between Italy and Sicily, Fig. 7a at 30 km down range (over the sill, cf. Fig. 6) there is a large section of negative flow (towards the Ionian Sea) of around 3 m s^{-1} . The yellow upper corners in the figure are modeling artifacts that represent continuation of the bathymetry by means of stagnant water; cf. discussion at the end of Section 3.4. Further down the x -axis at 60 km, between the sill and the Gulf of Gioia, the flow structure has a large section directed towards the sill, Fig. 7b, extending from the right to left boundaries and encompassing the bottom. The flow towards the sill on the right boundary reflects the inflow from the side boundary condition. On the left boundary there is flow towards the sill, also, in the lower layer. This indicates a local circulation. In the yz plane at 40 km down range (not shown), the flow away from the sill (in positive x direction) disappears and all the flow is towards the sill.

The flow is superposed on a sloping bottom that deepens as one proceeds away from the land into the sea. At the 60 km down range, Fig. 7c, the spanwise velocity indicates inflow along the ocean $y = L_y$ boundary where the barotropic forcing flow is prescribed (Section 3.4). The spanwise flow controls the negative flow away from the sill in the x -direction. When the semidiurnal tidal forcing reverses, the direction of flow on the sill and other locations reverses also.

4.3. Shoaling in the Gulf of Gioia

The solitary wave trains that are generated in the Strait of Messina region propagate into the Gulf of Gioia. Fig. 4 shows a solitary wave train, in the Gulf of Gioia area, approaching the shore over a rising topography. The flat region at the right represents continuation of the bathymetry by means of stagnant water; Section 3.4. At a time of 8.78 h the train has moved closer to shore, Fig. 8a. The initial soliton in the train has been slowed down by the topographic obstruction and the subsequent solitons are catching up with it. Eventually the solitons in the train are pushed together and one resultant depression is formed along the topography, Fig. 8b. This depression is slanted along the topographic rise. There is a pushing down of less dense water to depths of around 150 m from the surface over a horizontal extend of about 1–2 km. This opens the possibility for water mass modification through mixing. At a later time of 13.95 h the depression along the topography disappears and the isopycnals move up, towards their original equilibrium position, Fig. 8c. There remains a signature on the isopycnals to the left of the shore line suggesting reflectance effects. Reflectance effects have been observed by Guardiani et al. (1988).

In a horizontal plane at a depth of 100 m, the temperature field indicates the disturbances induced by the solitary waves and internal bores, Fig. 9. The plate (a) corresponds to Fig. 8a that shows the solitary wave

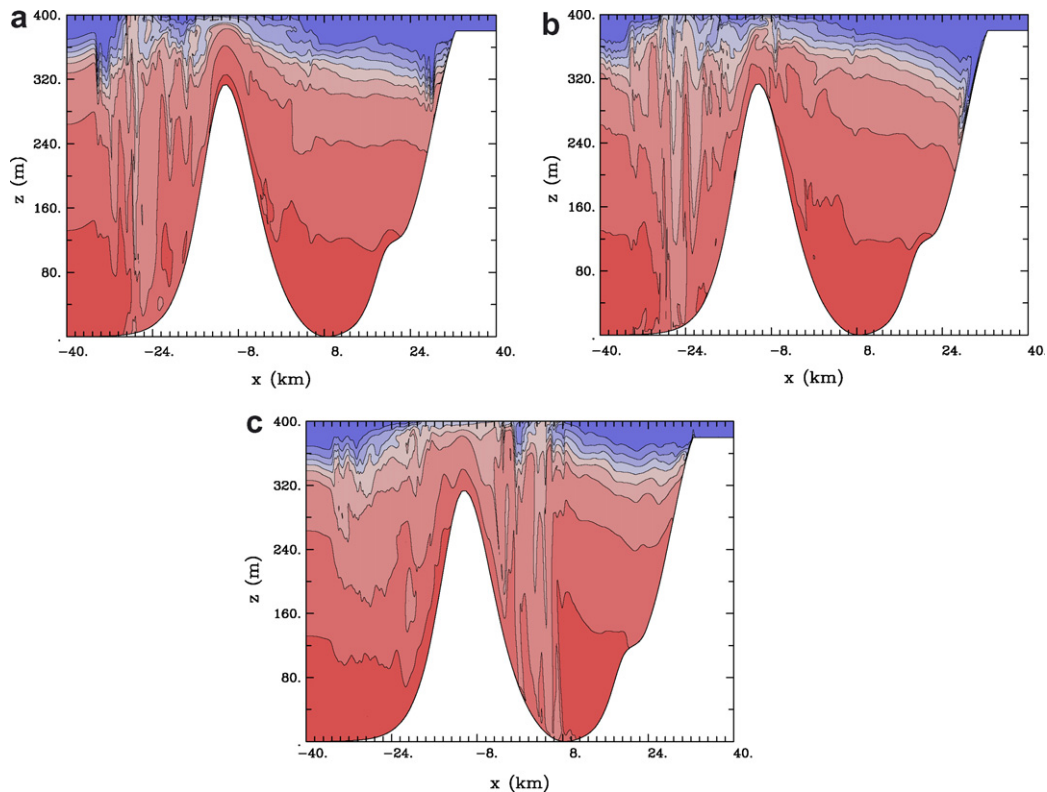


Fig. 8. Shoaling of a solitary wave train. Isohaline contours from 37.992 ppt to 38.638 ppt in intervals of 0.092 ppt in the $y = 5$ km (xz) plane at: (a) $t = 8.78$ h; (b) $t = 10.33$ h and (c) $t = 13.95$ h.

train about to shoal. Fig. 9a exhibits warmer temperatures caused by the solitary wave train depressions and a curvature of the solitary waves away from land, bottom of graph. At a time of 10.33 h, Fig. 9b, the depressions of the solitary waves line up along the shelfbreak slope and result in a warmer temperature there. At $t = 13.95$ h, Fig. 9c, the depressions along the shelfbreak slope have disappeared and the temperature distribution has returned towards its normal values.

We have introduced three moorings into the domain of the numerical experiment. The moorings were placed at 63, 68 and 69.5 km down range, in the middle (xz) plane at 5 km cross-range. The mooring at 68 km is centered in the leading depression of the shoaling solitary wave train shown in Fig. 8a at $t = 8.78$ h. The resultant temperature, salinity, and density distributions, at the moorings, are shown in Fig. 10 at the times of 8.78 h, 10.33 h, and 13.95 h. The density distribution for the mooring at 68 km down range, green curve, relative to the mooring at 63 km, blue curve. For $t = 10.33$ h, the time at which a large depression along the shelfbreak slope is evidenced in Fig. 8b, there are lighter density regions at depth for the mooring location of 68 and 69.5 km down range, green and red curves. This suggests mixing below the surface. At $t = 13.95$ h conditions relax towards normal.

Previously, Guardiani et al. (1988) have noted a patch of mixed water at mid depth in the Gulf of Gioia, during the JANE 1984 cruise. The patch was centered from 40 m to 100 m in depth. It was suggested that turbulent mixing due to breaking of internal waves could be the cause of a patch of mixed water. During the shoaling of internal wave trains, we do not observe internal wave breaking in the model predictions. The shoaling consist of solitary waves of the train piling up along an extended shelf slope causing a large depression that eventually return to equilibrium. What we do observe, however is a movement down of the surface water mass and a subsequent movement back up to the original position. This up and down movement causes water mass modifications through mixing, at depths of about 30 m to 150 m.

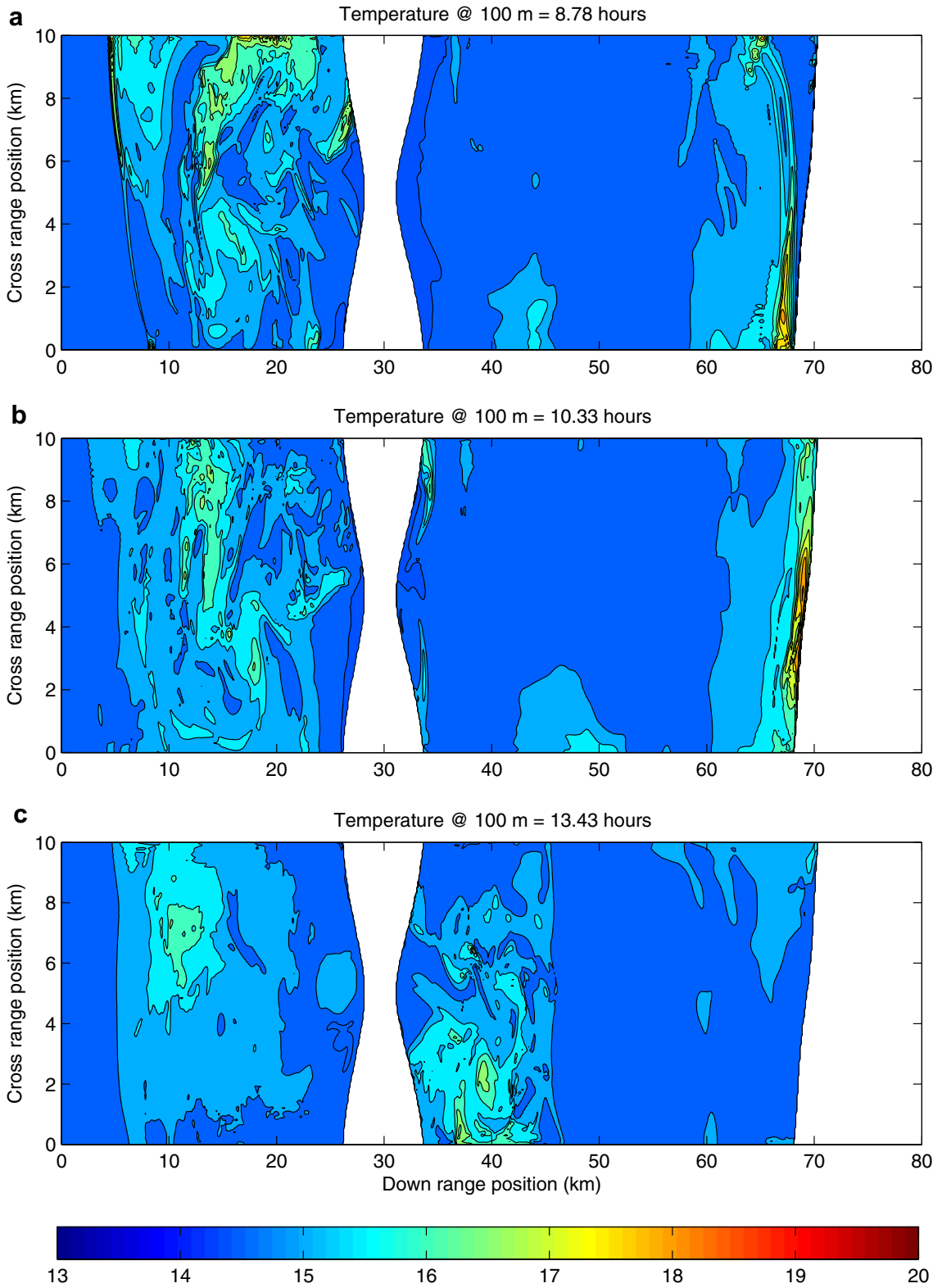


Fig. 9. Horizontal temperature distribution in a plane located 100 m below the surface at: (a) $t = 8.78$ h; (b) $t = 10.33$ h and (c) $t = 13.95$ h. Down range corresponds to the x -direction and cross-range to the y -direction.

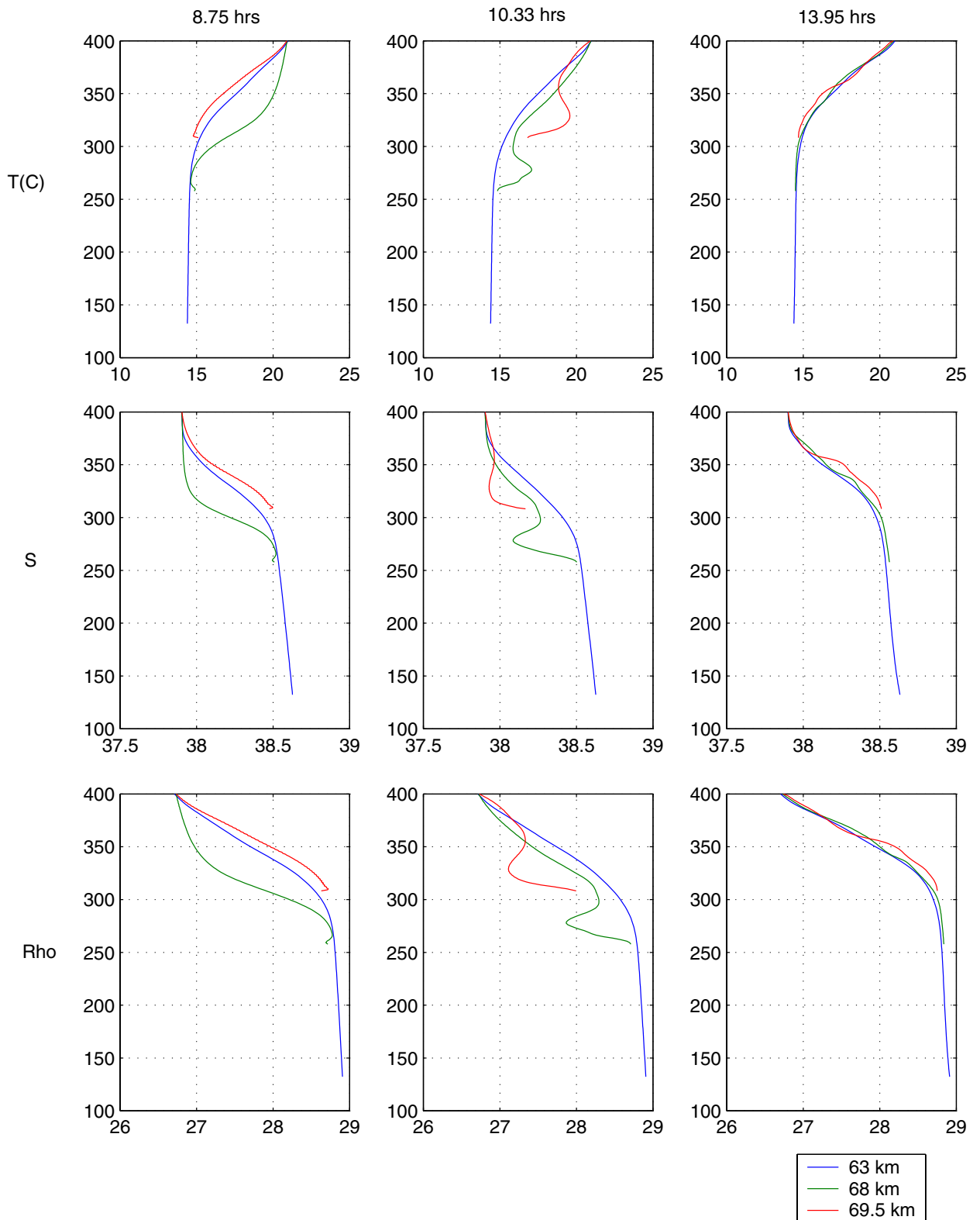


Fig. 10. Model predicted temperature, salinity, and density profiles for moorings located in the central (xz) plane at down range 63 km (blue curve), 68 km (green curve) and 69.5 km (red curve) for times $t = 8.78$ h, $t = 10.33$ h, and $t = 13.95$ h.

5. Comparisons with data and parameter sensitivities

5.1. Wavelet analysis of soliton packets

Traditionally researchers have relied on standard Fourier techniques to investigate the spectral composition of soliton packets. Nonetheless, because Fourier analysis gives signal amplitudes averaged over entire temporal or spatial domain, it is indiscriminating when a signal evolution is concerned. Unlike global Fourier decomposition, wavelet analysis expands one-dimensional time/space series into the two-dimensional parameter space (a, b) to provide a local measure of relative amplitude of activity at scale a and temporal or spatial location b (Meyers et al., 1993; Torrence and Compo, 1998). In order to obtain the characteristic scales and phase speeds exhibited by simulated soliton packets, we applied the wavelet analysis to isopycnal displacements in the pycnocline. We use the Morlet wavelet, proven successful in analyzing dispersion of Yanai waves in an ocean model (Meyers et al., 1993).

The analyzed signal, Fig. 11, represents a simulated soliton train in range (x -direction) consisting of 1024 grid points linearly interpolated from the model output to obtain a resolution of 10 m. The scale parameter a is varied to obtain wavelengths extending from 103 m to 2.81 km. Because the increase in sampling resolution is an artifact of the interpolation, the scales considered in practice range from a few 100 m to just over 2 km.

Consider the mid-thermocline displacement at $t = 6.2$ h in Fig. 11a. This is identically the result shown in Fig. 4a, however the range has been shifted in order to measure the solitary wave train from the sill and facilitate comparison to data. The contour indicates a train with several depressions. The wavelet power spectra of this train is shown in Fig. 11b. The figure exhibits the power as a function of range and wavelength. The absolute maximum intensity occurs at a wavelength near 1.33 km, the range location corresponding to the back side of the first depression at 31 km.² A tracking of the maximum power intensity as a function of wavelength is shown by the black curve in Fig. 11c, also referred to as the spine. It exhibits wavelengths ranging from about 0.75 km to 2 km, where intensities below the background intensity of 749.88 are not shown. The variation of the wavelengths along the spine over the contoured area show initial decrease of location in range as the small wavelengths increase to larger ones, Fig. 11c. This section of the spine contains large wavelength gradients. The variation reaches a minimum value in range, along the spine. The location of the minimum value in range is in the vicinity of large wavelength gradients, Fig. 11c. After the minimum, the range increases along the spine as the wavelengths increase.

The behavior of the spines at $t = 4.13$, 6.2, and 7.75 h are shown in Fig. 12b together with the model predicted soliton train structures in the pycnocline, Fig. 12a. The spines are shown as a function of wavelengths versus range; the range spans 20–45 km in order to show the evolving spine pattern. Each of the spines has a minimum range value. The wavelengths derived from the maximum wavelet power spectra vary as 1.16, 1.33, and 1.4 km, Table 2. The wavelength represents distances between troughs of the solitons. As time progresses the distance between the first two troughs of the soliton train tends to increase, Fig. 12a. The amplitude of the first soliton decreases from 52.3 m to 48.5 m from the first to the second location of the train. This follows the expected trend of decreasing amplitude in range. Then it increases somewhat, to 50.1 m, at the third location of the solitary wave train. This increase can be a fluctuation related to a decreasing ocean depth.

Along each spine the wavelengths increase from small to larger ones. High wavelength gradients occur along the spine slope as the wavelength increases up to minimum range value of the spine, Fig. 11c. The location of this section of the spine tends to extend to larger wavelengths as time progresses, Fig. 12b. Beyond the minimum range point along the spines, there are two dominant spine slopes with a transition region between them, Fig. 12b. The structure of the power distribution contours, Fig. 11c, also undergo changes as time progresses. The elliptical-like shape of power contour tends (not shown) to become more compressed along the wavelength distribution axis and more elongated in range as time increases. The major axis of the ellipse undergoes rotation and deformation. The deformation reflects the evolution of the soliton trains in time.

² Note that the range shift results in a roughly 11 km difference between Figs. 11 and 4a, where the first depression is located at about 20 km.

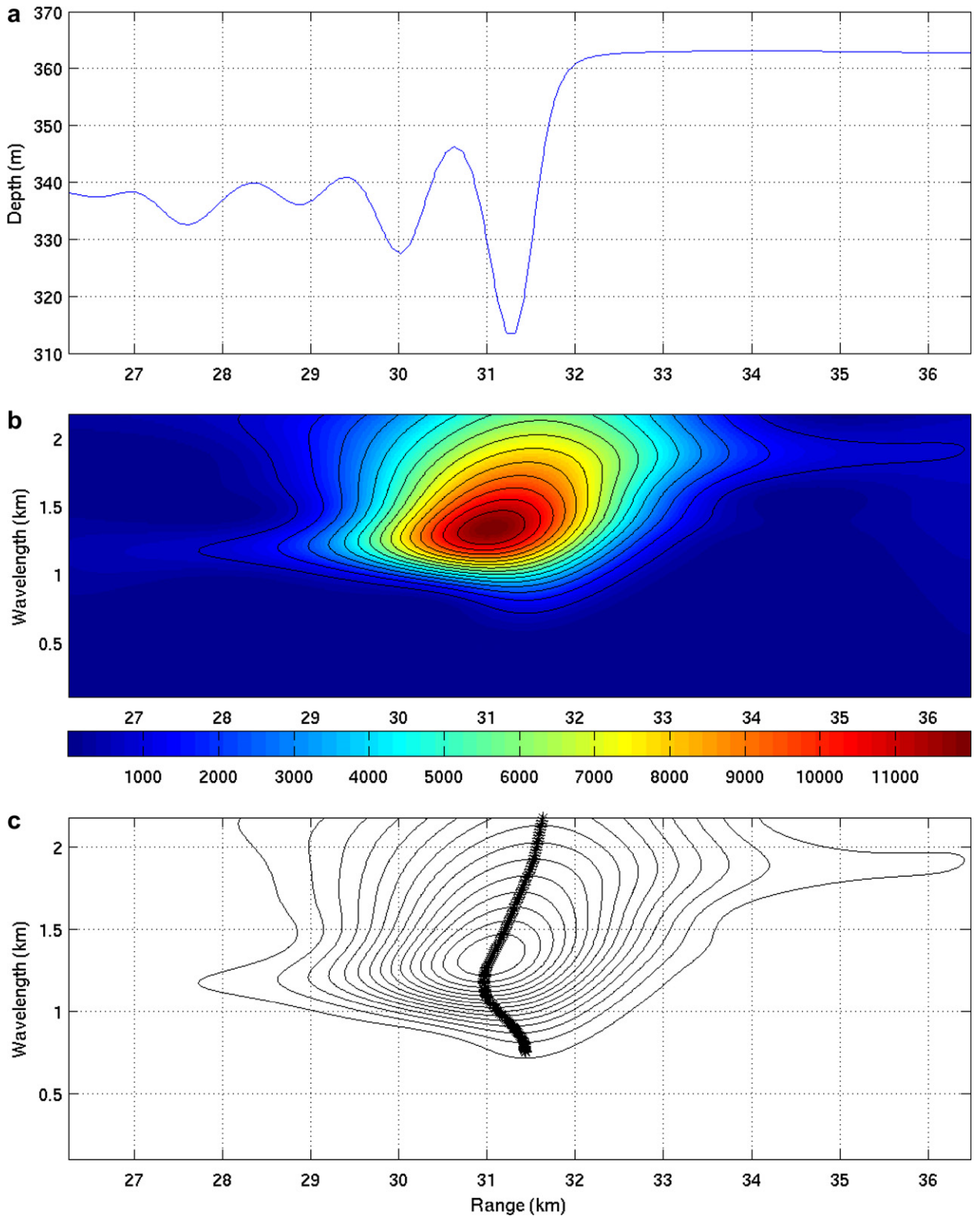


Fig. 11. (a) Model predicted mid-thermocline displacement at time of 6.2 h; (b) displacement intensity [m²] as a function of wavelength and range and (c) spine (black line) – i.e., maximum intensity for each wavelength – together with the intensity contours, which range from 749.88 to 11,248 and span 11.76 dB.

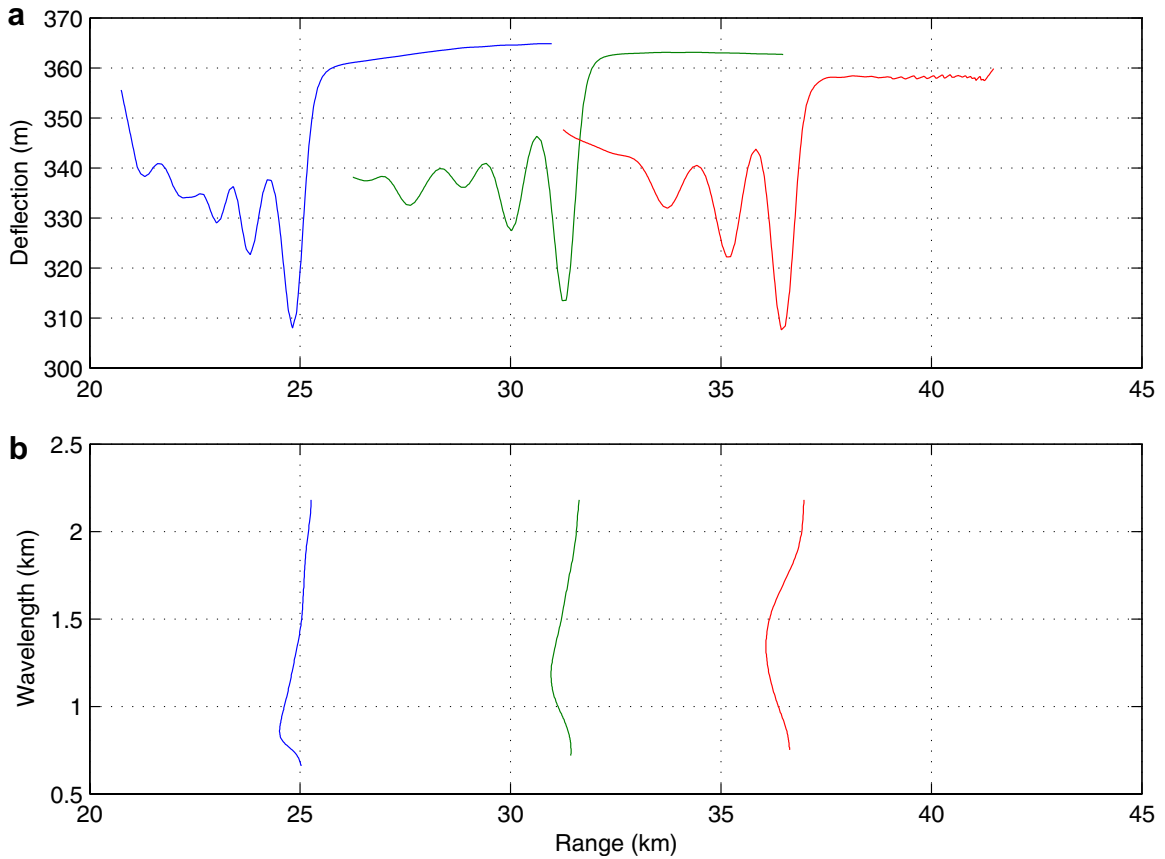


Fig. 12. Soliton evolution: (a) soliton trains as functions of depth and range at $t = 4.13$ h (blue), $t = 6.2$ h (green) and $t = 7.75$ h (red) using the mid-thermocline displacement and (b) the corresponding spines as a function of wavelength and range.

Table 2

Model predictions for case 1 in Table 1; λ_p is the wavelength corresponding to the maximum wavelet power spectra, A_1 is the amplitude of the 1st soliton and r is the range

Wavelength λ_p [km]	1.16	1.33	1.4
Amplitude A_1 [m]	52.3	48.5	50.1
Range r [km]	24.78	30.96	36.08

5.2. Comparisons with data characteristics

The evolution of the measured soliton wave trains over time and distance are compared with the evolution of the model predicted solitary wave trains. The CTD chain data described in Section 2 is used for comparing the model results. The range of the EULAG model predicted solitary wavetrains, Fig. 12a, are different from the ranges of the measured solitary wavetrains, Fig. 13a. The differences in ranges, or distances from the sill, of the model results and the measurements are due to the tidal phase used in initialization of the model results. The focus of the comparison is not on the range location but on changes over distance and time.

For the three CTD chain passes on the Tyrrhenian side, the mid-pycnocline displacement was extracted for the wavelet analysis. Table 3 lists the wavelengths, obtained through wavelet analysis, at maximum power for tows 5, 6, and 8 at ranges of 12.68, 15.65, and 20.67 km. The maximum power wavelength decreases in range and then increases. This is different from the model behavior, Table 2, where the wavelengths increase with

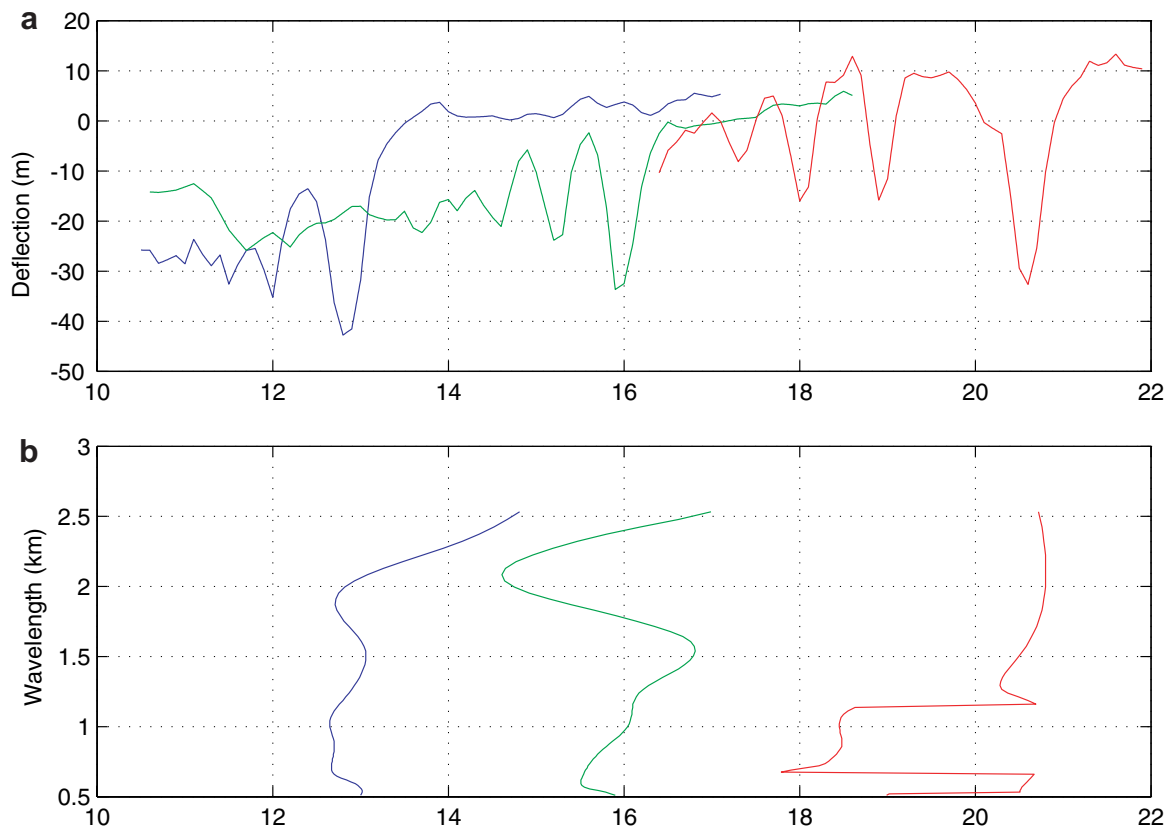


Fig. 13. (a) Measured soliton trains at $t = 616.83$ h (blue, tow 5), $t = 617.95$ h (green, tow 6), and $t = 619.47$ h (red, tow 8), and (b) corresponding spines as a function of wavelengths and range.

range. We attribute the behavior of wavelengths extracted from data to the presence of features in the ocean such as eddies that can compress and elongate the solitons.

The amplitude of the first soliton decreases from the first soliton train to the second, Table 3. From the second to the third train, the situation becomes more complicated. The first soliton's location and amplitude are influenced by a "feature", Fig. 13a. The location of the first soliton is advanced relative to the second and its amplitude increases relative to the second train. The magnitudes of the measured first soliton amplitudes, Table 3, are lower than the model predicted amplitudes, Table 2. For the first and third soliton trains the difference is around 6 m, with the model results being larger. For the second train the model results are about 15 m larger. This suggests some feature distortion, in the data for the amplitude of the first soliton in the second train.

The behavior of the spines as a function of range for each of the tows (5, 6 and 8) is shown in Fig. 13b together with the mid-pycnocline displacement, Fig. 13a. The spine for tow number 6, is reminiscent of the spine for tow number 5 with the modification of the initial minimum in range. Wavelengths below 0.5 km and above 2.5 km are in the power intensity background. For tow number 8, the spine has a discontinuous decrease in range for wavelengths ranging from about 0.7 km to 1.2 km, Fig. 13b. This discontinuous jump is associated with the solitary wave signal distortion that is visible in Fig. 13a, where the distance between the first and second depression is increased relative to tows number 5 and 6. This is caused by a feature.

The wavelengths tracked by the spines are measured by the tows and predicted by the model at certain times. A curve of wavelength as function of range and time can be obtained from the spine distributions. From the slope of these curves, the phase speeds are calculated as function of wavelength, solid blue curve in Fig. 14. The discontinuity in phase speed between the wavelengths of about 0.65 km and 1.1 km is evident and involves

Table 3

Results from data: λ_p is the wavelength corresponding to the maximum wavelet power spectra, A_1 is the amplitude of the 1st soliton and r is the range

Wavelength λ_p [km]	1.09	0.77	1.68
Amplitude A_1 [m]	46.58	33.3	44.57
Range r [km]	12.68	15.65	20.67

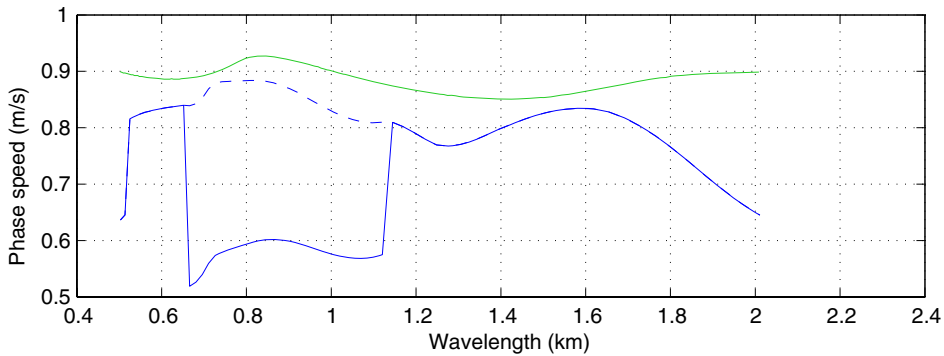


Fig. 14. Calculated phase speeds as a function of wavelength: green curve is derived from model predictions and blue curve from measurements.

a decrease in phase speed of about 0.25 m s^{-1} . This discontinuity can be caused by a feature that results in the advection, or stretching, of the first depression of the train away from the second depression, Fig. 13a. The other depressions in the soliton train can also be affected by the feature. Such a feature can be a local eddy with a velocity component along the solitary wave train. A correction for the movement due to advection can be introduced by moving the discontinuous portion of the phase speed curve up, dotted blue line in Fig. 14.

The model predicted phase speed, green curve in Fig. 14, has similar trends to the corrected measured phase speed curve. From wavelengths of 0.7 km to 1.6 km, the phase speeds increase up to a maximum, decrease, and then increase again. In the comparative range, the model phase speeds range from 0.93 m s^{-1} to 0.86 m s^{-1} and phase speeds derived from data range from 0.88 m s^{-1} to 0.77 m s^{-1} . For the comparative portion of the curve, the model results have somewhat higher phase speeds and a slightly different dispersion versus wavelength variation. The overall phase speed trends are similar between model and data. For the non-comparative portions of the curves – below wavelengths of 0.7 km and above 1.6 km – the phase speed trends of model predictions and data are different. These are the portions where the power intensity distribution in wavelength and range merges with the background; cf. Fig. 11b.

Sapia and Salusti (1987) observed internal solitary waves in the Strait of Messina and derived theoretical estimates of linear and nonlinear phase speeds from hydrography measurements. On the north side of the strait the linear phase speed estimate was 0.6 m s^{-1} and the nonlinear 0.72 m s^{-1} . These calculations are dependent on the measured density and the application of a two-layer approximation. Measurement with a towed temperature sensor yielded nonlinear phase speed estimates of 0.8 m s^{-1} . Phase speeds of 0.8 m s^{-1} are in the range of the phase speeds derived from the present data sets.

5.3. Parameter variations

We have varied the initial conditions and the magnitude of the semidiurnal barotropic tidal forcing. Table 1 lists the parameters variations that we considered. Left and right plates in Fig. 2 illustrate the initial temperature and salinity profiles, respectively, that were used for model initializations.

A comparison of derived phase speed as a function of wavelength for different parameters is shown in Fig. 15. Cases 1 and the data are the same as in Fig. 14. Case 2 represents a lower barotropic tidal forcing.

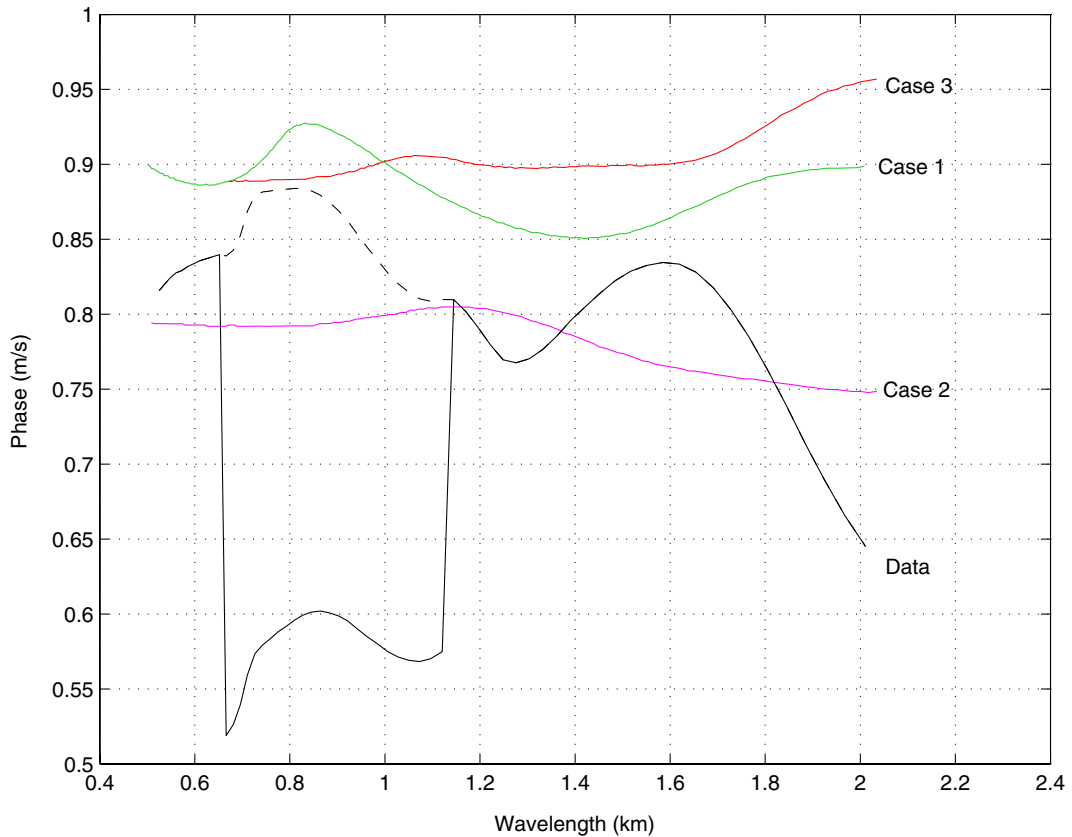


Fig. 15. Phase speed as a function of wavelength for different parameters. Table 1 lists the model parameters for the cases. Case 1 and data phase speeds are as in Fig. 14.

The predicted phase speeds versus wavelength are smaller than those for case 1. A lower tidal forcing, results in less isopycnal displacement, retardation in solitary wave formation, and smaller tidal background velocity (Lamb, 1994; Warn-Varnas et al., 2003). As a result the phase velocities are smaller. Case 3 represents deeper thermocline and haloclines. The phase speed has an increasing trend and for wavelengths exceeding 1 km is larger than those of case 1. For wavelengths from about 0.65 km to 1 km, the phase speed is smaller than in case 1 and closer to the data, Fig. 15. The phase speed variation versus wavelength exhibits less variation than case 1 or the data. Case 1 and the data show an increase, a decrease, and an increase again to about wavelengths of 1.6 km. Case 1 exhibits more of the data trends than case 2 and 3.

The wavelengths derived from wavelet analysis are summarized in Table 4 for the three cases. Case 1 indicates wavelengths ranging from 1.16 km to 1.4 km. Case 3 wavelengths range from 1.25 km to 2.18 km. Case 3 wavelengths are correspondingly larger for each of the three solitary wave trains. The deeper thermocline and halocline locations of case 3 lead to larger wavelengths in relation to case 1. The first soliton amplitudes for case 3, Table 4, are larger for the second and third solitary wave trains than the corresponding amplitudes for case 1. For the first soliton train the amplitude is smaller for case 3 than in case 1. The first soliton could still be in the development stage.

In Case 2, the lower tidal forcing at the boundary results in decreasing wavelengths from the first to the third solitary wave trains, Table 4. A lower tidal forcing results in smaller internal bores that disintegrate into wider width solitons. The corresponding amplitudes of the first soliton increase for the first train to the second and then decrease in the third train. The magnitude of the amplitudes are smaller than those for case 1, case 2 and the data. A smaller tidal velocity leads to smaller displacements of isopycnals and smaller amplitudes for the solitons. The tidal forcing magnitude of case 2 does not lead to amplitudes close to those observed in the data.

Table 4

Model prediction summary: λ_p is the maximum power spectra wavelength, A_1 is the amplitude of the 1st soliton and r is the range

Case	λ_p [km]	A_1 [m]	r [km]
1	1.16	52.3	24.78
	1.33	48.5	30.96
	1.4	50.1	36.08
2	2.18	17.49	20.40
	2.05	23.87	25.71
	1.9	21.32	29.78
3	1.25	43.9	25.65
	1.67	52.1	33.1
	2.18	51.27	38.56

6. Acoustical effects

From an acoustic point of view the interesting part of this study was the 3D aspects of the modeled ocean environment. The ocean model results covered an area of 10 km by 80 km. This area is shown by the dashed box of Fig. 1.

Acoustic model simulations were used to illustrate the effects of a 3D ocean environment as compared to the acoustic effects of a 2D environment. The acoustic simulations were made using the finite element parabolic equation (FEPE) model (Collins, 1988a; Collins, 1988b; Collins and Westwood, 1991). The FEPE model gives accurate, wave-theoretic, numerical predictions of acoustic pressure at all forward propagating angles about the direction of propagation. Since the model uses a marching solution technique taken at intervals that are a fraction of the acoustic wavelength, the model is ideal for accurately including small ocean environmental changes, and their effects (refraction, diffraction, interference) on the acoustic field. The FEPE model has been verified as benchmark accurate (Collins, 1990); thus, it was an appropriate choice for these simulations.

Three tracks were chosen that would illustrate the acoustic effects of the simulated 3D ocean environment in Fig. 3d. One track was in the middle of the ocean area (designated as “Center”). One track was parallel to the Center track and displaced 4 km to the west (designated as “West”) of the Center track. One track was parallel to the center and displaced 4 km to the east (designated as “East”). These three tracks traversed parallel, adjacent ocean environments that were oriented from the northeast to southwest (refer to Fig. 1). The

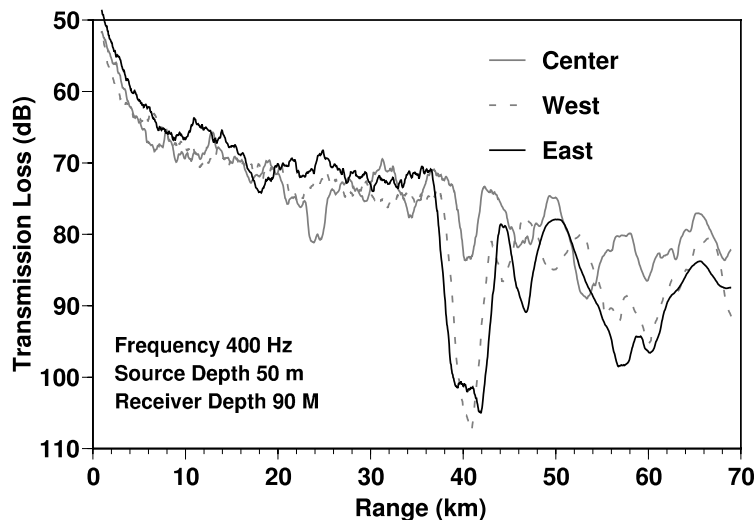


Fig. 16. Transmission loss vs. range plot for the Center (gray line), West (dashed line) and East (solid black) tracks for a frequency of 400 Hz, source depth 50 m and receiver depth of 90 m.

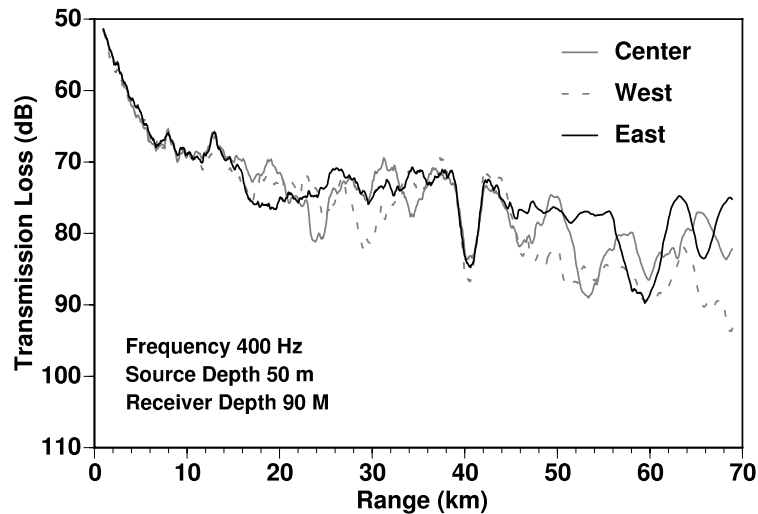


Fig. 17. Transmission loss vs. range for the same three tracks shown in Fig. 16, but with the bathymetry the same for all three tracks.

starting location is in the Gulf of Gioia and going southwest. A source depth of 50 m was selected for each track and the start range for each track made to correspond to with the 70 m depth contour line.

Fig. 16 shows the results of the acoustic model simulation. The vertical axis is acoustic transmission loss in decibels (referenced to 1 m). The horizontal axis is the range in km. The acoustic source is at a frequency of 400 Hz, and the receiver depth is 90 m. The transmission loss for the center track is represented by the gray curve. The dotted line is transmission loss for the parallel track that is 4 km to the west. The solid black line is the parallel track 4 km to the east. The three transmission loss curves show differences over the whole range with the most notable at about 40 km where differences of nearly 20 dB are evident. This large discrepancy is due to the different bathymetry along each track. The strait is located around 40 km in range and the bathymetry depth at that range is less for the East and West tracks than for the Center track. Thus, to a large degree, the differences in the bathymetry are contributing to the differences in transmission loss between the three tracks.

To isolate the effects of the 3D sound speed field, the bathymetry was made the same for all three tracks, Center, West and East. The Center track bathymetry was used for all three tracks. The results of this set of simulations is show in Fig. 17. With the bathymetry the same for all three tracks, the only environmental difference left is due the three dimension effects of the sound speed field. The transmission loss in Fig. 17 shows that the environments for the three tracks are acoustically similar up to a range of about 14 km, where the effects of the difference in the sounds speed fields are beginning to modify the transmission loss. After the acoustic track passes the sill the differences become even more pronounced.

This simple acoustic simulation helps to demonstrate the acoustic impact of accounting for the 3D aspects of the oceanography. Ignoring the variation in the sound speed field can produce significant differences in the acoustic propagation.

7. Conclusions

Three-dimensional simulations of the Strait of Messina and Gulf of Gioia region were conducted with the newly developed and documented ocean version of nonhydrostatic model EULAG, proven successful in simulating a variety of rotating stratified flows. The simulation were initialized from measured temperature and salinity profiles and forced by the existing semidiurnal tidal magnitudes obtained from a tidal model. The simulation showed that as the semidiurnal tide moves over the sill in the Strait of Messina, it generates a depression. The depression results in right and left propagating waves that form internal bores. During tidal reversals, the formed bores undergo hydraulic jumps over the sill and salinity and temperature fronts develop.

The fronts are defined by the internal bore boundaries. Over the sill the interface formed by the front separates water masses. The interface can be located anywhere between the surface and the sill.

The internal bores that propagate away from the sill, steepen on the leading edge through nonlinear effects and disintegrate into solitary wave trains as amplitude and frequency dispersion set in. This has been shown previously with a 2D layer model by Brand et al. (1997). The propagating solitary wave trains towards the Gulf of Gioia exhibit curvature effects in horizontal planes. In the Gulf of Gioia, the solitary wave trains shoal. In the shoaling process a depression is formed along the Gulf of Gioia slope. The depression pushes less dense surface water to depths of about 150 m. Moorings placed in the model predictions indicate the presence of lighter water at depths below the surface during the shoaling of solitary wave trains in the Gulf of Gioia. This suggests mixing of water masses at depth. Mixed patches of water have been observed by Guardiani et al. (1988), in the Gulf of Gioia, during the JANE 1984 cruise.

The model results and data were compared by conducting a wavelet analysis. The wavelengths were tracked by the spines (maximum intensity for each wavelength) at various times. From the slope of the variations, phase speed were derived as a function of wavelength. For the parameters extracted from CTD measurements and existing tidal conditions, phase speed distributions for wavelengths ranging from about 0.6 m to 1.6 km were obtained. A correction for feature distortion was applied to the last tow of the measured soliton phase speed distribution. The model predicted phase speed versus wavelength had similar trends to the phase speed derived from data. The model predicted phase speed magnitudes ranged from 0.88 m s^{-1} to 0.93 m s^{-1} . The phase speeds derived from data ranged from 0.77 m s^{-1} to 0.88 m s^{-1} . Model predicted wavelengths and amplitudes were within 15% of CTD chain measurements.

Parameters of thermocline and halocline depths were varied from the measured conditions at the CTD station by increasing them. The semidiurnal tidal forcing was also varied by reducing it to half of the extracted barotropic tidal forcing at the boundary. A variation of the tidal parameter to half, yielded a lower model predicted phase velocity distribution versus wavelength. The magnitude of the phase velocity ranged from about 0.805 m s^{-1} to 0.75 m s^{-1} and exhibited a different wavelength dependence from the larger tidal parameter case. An increase of the thermocline and halocline depth parameters yielded a higher phase speed versus wavelength for wavelengths greater than 1 km. The phase speed as a function of wavelength had an increasing trend as the wavelength increased.

Finally, the acoustic predictions using a 3D ocean environment can be significantly different when compared with similar acoustic predictions using a 2D ocean environment. In our simulations, even with bathymetry effects removed, 5 dB differences in acoustic signals were observed over a range of 70 km.

Acknowledgements

We gratefully acknowledge the many helpful suggestions made by various colleagues. This work was supported by the Office of Naval Research under PE 62435N, with technical management provided by the Naval Research Laboratory; and by the Department of Energy (DOE) Climate Change Prediction Program (CCPP). NCAR is sponsored by the National Science Foundation.

Appendix. Numerical apparatus

Given (7), the prognostic Eqs. (3)–(5) can be written in the symbolic form of an Eulerian conservation law

$$\frac{\partial \rho^* \psi}{\partial t} + \nabla \cdot (\rho^* \mathbf{v}^* \psi) = \rho^* R, \quad (16)$$

where ψ symbolizes components of \mathbf{v} , ρ' , or s and R denotes the associated rhs. The archetype problem (16) is approximated to second-order accuracy in space and time using an NFT algorithm

$$\psi_i^{n+1} = \mathcal{A}_i(\tilde{\psi}) + 0.5 \Delta t R_i^{n+1} \equiv \hat{\psi}_i + 0.5 \Delta t R_i^{n+1}; \quad (17)$$

where ψ_i^{n+1} is the solution sought at the grid point $(\bar{t}^{n+1}, \bar{\mathbf{x}}_i)$, $\tilde{\psi} \equiv \psi^n + 0.5 \Delta t R^n$, and \mathcal{A} denotes a two-time-level flux-form Eulerian nonoscillatory advective-transport operator MPDATA; see Smolarkiewicz (2006) for a recent overview.

Eq. (17) represents a system implicit with respect to all dependent variables in (3) and (4), because all forcing terms are assumed to be unknown at $n + 1$. Notably, the salinity Eq. (5) has zero right-hand side, whereupon s has a status of a passive scalar. For the physical velocity vector \mathbf{v} , (17) can be written compactly as

$$\mathbf{v}_i = \hat{\mathbf{v}}_i - 0.5\Delta t(\tilde{\mathbf{G}}(\bar{\nabla}\pi'))_i + 0.5\Delta t\mathbf{R}_i(\mathbf{v}, \hat{\rho}'), \quad (18)$$

where

$$\mathbf{R}_i(\mathbf{v}, \hat{\rho}') \equiv \mathbf{g} \frac{1}{\rho_0} (\hat{\rho}'_i - 0.5\Delta t((\tilde{\mathbf{G}}^T \mathbf{v}) \cdot \bar{\nabla} \rho_c)_i) - (\mathbf{f} \times (\mathbf{v} - \mathbf{v}_c))_i \quad (19)$$

accounts for the implicit representation of the buoyancy via (4), and the superscript $n + 1$ has been dropped as there is no ambiguity. Given a grid co-located with respect to all prognostic variables, (18) can be inverted locally to construct expressions for the solenoidal velocity components that are subsequently substituted into (2) to produce an elliptic equation for pressure

$$\left\{ \frac{\Delta t}{\rho^*} \bar{\nabla} \cdot \rho^* \tilde{\mathbf{G}}^T [\hat{\mathbf{v}} - (\mathbf{I} - 0.5\Delta t \hat{\mathbf{R}})^{-1} \tilde{\mathbf{G}}(\bar{\nabla}\pi'')] \right\}_i = 0, \quad (20)$$

where $\tilde{\mathbf{G}}^T[\hat{\mathbf{v}} - (\mathbf{I} - 0.5\Delta t \hat{\mathbf{R}})^{-1} \tilde{\mathbf{G}}(\bar{\nabla}\pi'')] \equiv \bar{\mathbf{v}}^s$ defined in (6), and the additional hats and prime denote straightforward algebraic modifications; cf. Prusa and Smolarkiewicz (2003) for the complete exposition. Boundary conditions imposed on $\bar{\mathbf{v}}^s \cdot \mathbf{n}$, subject to the integrability condition $\int_{\partial\Omega} \rho^* \bar{\mathbf{v}}^s \cdot \mathbf{n} d\sigma = 0$, imply the appropriate boundary conditions on π'' (Prusa and Smolarkiewicz, 2003; Wedi and Smolarkiewicz, 2004). The resulting boundary value problem is solved using a preconditioned generalized conjugate residual GCR(k) algorithm (Eisenstat et al., 1983); for further discussion, see Smolarkiewicz et al. (2004) and references therein. Given the updated pressure, and hence the updated solenoidal velocity, the updated physical and contravariant velocity components are constructed from the solenoidal velocities using transformations (8) and (6), respectively.

References

- Alpers, W., Salusti, E., 1983. Scylla and Charybdis observed from space. *Journal of Geophysical Research* 88, 1800–1808.
- Benoit, Cushman-Roisin, 1994. *Introduction to Geophysical Fluid Dynamics*. Prentice Hall, Englewood Cliff, New Jersey 07632.
- Brand, P., Alpers, W., Rubino, A., Backhaus, J., 1997. Internal waves in the Strait of Messina studied by a numerical model and synthetic aperture radar images from the ERS Satellites. *Journal of Physical Oceanography* 27 (5), 648–663.
- Collins, M.D., 1988a. Low-frequency, bottom-interacting pulse propagation in range-dependent oceans. *IEEE Journal of Oceanic Engineering* 13, 222–228.
- Collins, M.D., 1988b. FEPE users guide. NORDA TN-365. Naval Research Laboratory, Stennis Space Center, MS, USA.
- Collins, M.D., 1990. Benchmark calculations for higher-order parabolic equations. *Journal of the Acoustical Society of America* 87, 1535–1538.
- Collins, M.D., Westwood, E.K., 1991. A higher-order energy-conserving parabolic equation for range-dependent ocean depth, sound speed, and density. *Journal of the Acoustical Society of America* 89, 1068–1074.
- Del Ricco, R., 1981. Numerical model of the internal circulation of a strait under the influence of the tides. Applications to the Strait of Messina. Thesis at the Institute of Physics, University of Rome.
- Eisenstat, S.C., Elman, H.C., Schultz, M.H., 1983. Variational iterative methods for nonsymmetric systems of linear equations. *SIAM Journal of Numerical Analysis* 20, 345–357.
- Gal-Chen, T., Somerville, C.J., 1975. On the use of a coordinate transformation for the solution of the Navier–Stokes equations. *Journal of Computational Physics*. 17, 209–228.
- Guardiani, G., Pace, A., Salusti, E., 1988. Preliminary observations of turbulence due to the collapse of internal solitary waves in the Gulf of Gioia, north of the Strait of Messina. *Bollettino di Oceanologia Teorica ed Applicata* VI (1), 3–14.
- Hopkins, T.S., Salusti, E., Settini, D., 1984. Tidal forcing of the water mass interface in the Strait of Messina. *Journal of Geophysical Research* 89, 2013–2024.
- JANE 84, 1985. Istituto di Fisica G. Marconi, Universita di Roma La Sapienza in collaborazione con IFA-CNR, Preprint No. 433, 15 Gennaio.
- Lamb, K., 1994. Numerical experiments of internal wave generation by strong tidal flow across a finite amplitude bank edge. *Journal of Geophysical Research* 99 (C1), 848–864.
- Marshall, J., Hill, C., Perelman, L., Adcroft, A., 1997. Hydrostatic, quasi-hydrostatic, and nonhydrostatic ocean modeling. *Journal of Geophysical Research* 102 (C3), 5733–5752.

- Martin, P.J., 2000. A description of the navy coastal ocean model version 1.0. NRL Report NRL/FR/732200-9962, Naval Research Laboratory, SSC, MS 39529, 42 pp.
- Meyers, S.D., Kelly, B.G., O'Brien, J.J., 1993. An introduction to wavelet analysis in oceanography and meteorology with application to the dispersion of Yanai wave. *Monthly Weather Review* 121, 2858–2866.
- Osborne, A.R., Burch, T.L., 1980. Internal solitons in the Andaman Sea. *Science* 280, 451–460.
- Prusa, J.M., Gutowski, W.J., 2006. MPDATA and grid adaptivity in geophysical fluid flow models. *International Journal for Numerical Methods in Fluids* 50, 1207–1228.
- Prusa, J.M., Smolarkiewicz, P.K., 2003. An all-scale anelastic model for geophysical flows: dynamic grid deformation. *Journal of Computational Physics* 190, 601–622.
- Prusa, J.M., Smolarkiewicz, P.K., Wyszogrodzki, A.A., 2001. Simulations of gravity wave induced turbulence using 512 PE CRAY T3E. *International Journal of Applied Mathematics and Computer Science* 11 (4), 883–897.
- Sapia, A., Salusti, E., 1987. Observation on nonlinear internal solitary wave trains at the northern and southern mouths of the Strait of Messina. *Deep-Sea Research* 34, 1081–1092.
- Sellschopp, J., 1997. A towed CTD chain for high-resolution hydrography. *Deep Sea Research* 44, 147–165.
- Smolarkiewicz, P.K., 2006. Multidimensional positive definite advection transport algorithm: an overview. *International Journal for Numerical Methods in Fluids* 50, 1123–1144.
- Smolarkiewicz, P.K., Margolin, L.G., 2007. Studies in Geophysics. Chapter 14 in *Implicit large eddy simulation: computing turbulent fluid dynamics*. In: Grinstein, F.F., Margolin, L., Rider W. (Eds.), Cambridge University Press, to appear.
- Smolarkiewicz, P.K., Prusa, J.M., 2002. Forward-in-time differencing for fluids: simulation of geophysical turbulence. In: Drikakis, D., Guertz, B.J. (Eds.), Chapter 8 in *Turbulent Flow Computation*. Kluwer Academic Publishers, pp. 279–312.
- Smolarkiewicz, P.K., Prusa, J.M., 2005. Toward mesh adaptivity for geophysical turbulence: continuous mapping approach. *International Journal for Numerical Methods in Fluids* 47, 789–801.
- Smolarkiewicz, P.K., Margolin, L.G., Wyszogrodzki, A.A., 2001. A class of nonhydrostatic global models. *Journal of the Atmospheric Sciences* 58, 349–364.
- Smolarkiewicz, P.K., Temperton, C., Thomas, S.J., Wyszogrodzki, A.A., 2004. Spectral preconditioners for nonhydrostatic atmospheric models: extreme applications. In: *Proceedings of the ECMWF Seminar Series on Recent Developments in Numerical Methods for Atmospheric and Ocean Modelling*, 6–10 September 2004, Reading, UK, pp. 203–220.
- Sterneck, R., 1915. *Hydrodynamische Theorie der halbtaegigen Gezeiten des Mittelmeeres*. Sitz. Berich. d.k.k. Akad. Wien.
- Temam, R., 2006. Suitable initial conditions. *Journal of Computational Physics* 218, 443–450.
- Torrence, C., Compo, G.P., 1998. A practical guide to wavelet analysis. *Bulletin of the American Meteorological Society* 79, 61–78.
- Vercelli, F., 1925. Il regime delle correnti e delle mare nello Stretto di Messina. *Commissione Internazionale del Mediterraneo*, Venezia, 135pp.
- Warn-Varnas, A., Chin-Bing, S.A., King, D.B., Hallock, Z., Hawkins, J., 2003. Ocean-acoustic solitary wave studies and predictions. *Surveys in Geophysics* 24, 39–79.
- Wedi, N.P., 2006. The energetics of wave-driven mean flow oscillations. *International Journal for Numerical Methods in Fluids* 50, 1175–1191.
- Wedi, N.P., Smolarkiewicz, P.K., 2004. Extending Gal-Chen and Somerville terrain-following coordinate transformation on time-dependent curvilinear boundaries. *Journal of Computational Physics* 193, 1–20.
- Wedi, N.P., Smolarkiewicz, P.K., 2006. Direct numerical simulation of the Plumb–McEwan laboratory analogue of the QBO. *Journal of the Atmospheric Sciences* 63, 3226–3252.